http://dx.doi.org/10.21577/0103-5053.20170061

J. Braz. Chem. Soc., Vol. 28, No. 9, 1803-1815, 2017.
Printed in Brazil - ©2017 Sociedade Brasileira de Química
0103 - 5053 $6.00+0.00

Article

Investigation of Electrocatalysts for Selective Reduction of CO_2 to CO: Monitoring the Reaction Products by on line Mass Spectrometry and Gas Chromatography

Mariana R. Camilo, Wanderson O. Silva and Fabio H. B. Lima*

Instituto de Química de São Carlos, Universidade de São Paulo (USP), CP 780, 13560-970 São Carlos-SP, Brazil

The carbon dioxide electrocatalytic reduction is central for the development of regenerative cycles of electrochemical energy conversion and storage. Herein, the gaseous products of the CO_2 electroreduction were monitored by using an electrochemical cell on line coupled to a differential electrochemical mass spectrometer (DEMS), aiming at searching for electrocatalysts with high selectivity for CO formation. The results showed that, among the studied materials, the Cu_4Sn/C alloy nanoparticles were stable during potentiostatic polarizations as revealed by *in situ* X-ray absorption spectroscopy (XAS), and the on line DEMS measurements showed the production of CO, suppression of methane and ethylene formations, and diminishing of the hydrogen evolution reaction, in relation to that on pure Cu_2O-Cu/C. The faradaic efficiencies for CO formation were 13 and 23% for Cu_4Sn/C and Au/C (a known electrocatalyst for CO), respectively, determined by experiments of in line gas chromatography (GC). The selectivity of Cu_4Sn/C for CO formation was ascribed to the role of Sn atoms on stabilizing adsorbed HCOO intermediates, and hindering further hydrogenation, letting CO free for desorption. These results are expected to be used as a guide for further development of electrocatalysts with a fine-tuning of composition for increasing the faradaic efficiency of CO_2 electroreduction to CO.

Keywords: CO_2 electrochemical reduction, on line DEMS, in line GC, CO formation, Cu_4Sn/C alloy

Introduction

Concomitantly with the growth of the world population, the energy demand is increasing. To satisfy this scenario, fossil fuels, such as oil, coal and natural gas, are being exhaustively used. Unfortunately, together to the dependence on these fuels, large amounts of carbon dioxide (CO_2) are emitted into the environment and, so, this is not a sustainable cycle. This has initiated research projects to investigate efficient processes for using the available CO_2 in the atmosphere. The electrochemical reduction of carbon dioxide is, in principle, an efficient manner that can be explored. In this context, the electroreduction of CO_2 to fuels with high-energy density or to industrial chemicals, that can be further processed to produce useful fuels, such as CO, using photovoltaic panels, with the consecutive utilization as fuel in fuel cells, would define a sustainable or regenerative cycle.[1-7] In the case of performing the CO_2 electroreduction to CO in parallel with the water electroreduction (or the hydrogen evolution reaction (HER)), the mixture CO + H_2 (syngas) is produced.[8,9] In the chemical industry, CO/H_2 mixtures are reacted to form methanol or other liquid fuels, such as diesel, by using the Fischer-Tropsch process.[10]

The CO_2 electrochemical reduction can be product-selective by using different electrocatalysts. However, even for two-electron products, it is decisive to know the kinetically important steps of the studied reaction. Also, synthesizing an optimized electrocatalyst that do not catalyze undesirable parallel reactions is a difficult task.[11] The CO_2 electroreduction in aqueous electrolyte, and at pH 7.0, utilizes water as the proton source. Additionally, even for the same number of electrons, different products can be produced, e.g., the two-electron pathway can generate CO and/or $HCOO^-$ (equations 1 and 2). More complex routes, involving multiple steps of hydrogen addition, are possible, and this is the case of methane and ethylene formation (equations 3 and 4, respectively):

$$CO_2 + H_2O + 2\,e^- \rightarrow HCOO^- + OH^- \quad (-0.43\ V) \quad (1)$$

$$CO_2 + H_2O + 2\,e^- \rightarrow CO + 2\,OH^- \quad (-0.52\ V) \quad (2)$$

*e-mail: fabiohbl@iqsc.usp.br

$$CO_2 + 6\ H_2O + 8\ e^- \rightarrow CH_4 + 8\ OH^- \quad (-0.25\ V) \quad (3)$$

$$2\ CO_2 + 8\ H_2O + 12\ e^- \rightarrow C_2H_4 + 12\ OH^- \quad (-0.34\ V) \quad (4)$$

potentials *vs.* standard hydrogen electrode (SHE)

As can be seen, the equilibrium potentials of the electrochemical reduction of CO_2 are not very negative when compared to that of water electroreduction (equation 5, below). However, experimentally, high overpotentials are needed, even for the two-electron routes. In literature, this fact is related to the low potential (–1.9 V) for the single electron reduction of carbon dioxide to the radical anion $CO_2^{\bullet-}$ ($CO_2 + e^- \rightarrow CO_2^{\bullet-}$), and this may be the activation of CO_2 for subsequent reduction steps.

Due to the low potential of this activation step, in aqueous conditions, the hydrogen evolution reaction (equation 5, HER) takes place in parallel to the CO_2 electroreduction:

$$2\ H_2O + 2\ e^- \rightarrow H_2 + 2\ OH^- \quad (-0.41\ V) \quad (5)$$

The challenges for the electrocatalytic CO_2 reduction are related to the product selectivity or faradaic efficiency. However, it depends on several different experimental conditions such as applied potential, concentration of the reactants, electrolyte composition, temperature and electrocatalyst.[12] Metallic electrocatalysts have been commonly investigated in aqueous electrolyte such as gold,[13-15] copper,[16-19] tin,[20] silver[21,22] and nickel,[23] and they are classified according to their hydrogen evolution overpotentials and CO adsorption strength:[24] (*i*) metals such as Pb, Hg, In, Sn, Cd and Bi have high hydrogen overvoltages, negligible CO adsorption strength, high overpotentials for CO_2 to $CO_2^{\bullet-}$, and weak stabilization of $CO_2^{\bullet-}$, and they produce $HCOO^-$ as the major product; (*ii*) Au and Ag have medium hydrogen overpotential, and weak CO adsorption properties, and their major product is CO; (*iii*) Ni, Fe and Pt have low hydrogen overpotentials and strong CO adsorption, and the major product is H_2 (water electroreduction); (*iv*) Cu is single in this group and is able to reduce CO_2 to more reduce species such as CH_4 and C_2H_4.[19,25-31]

For copper, its ability for hydrocarbon formation is mainly associated to its moderate CO binding energy, which leads Cu to sit near to the top of a volcano type relation of the limiting-potentials curves of $CO_2 \rightarrow$ COOH* and CO* $\rightarrow$ CHO* steps (*: adsorption site) as a function of the CO binding energy, as discussed by Peterson and Nørskov.[32] For Pt and Ni, for example, HER dominates over the CO_2 reduction. CO is bound very tightly to these metals, and the removal of this CO_2 reduction intermediate requires its protonation, which form COH* rather than CHO*, changing the reaction pathway. Au and Ag bind CO very weakly, so they are far from the top of the volcano curve, and sit to the right of the binding energy at which adsorbed CO (*CO) is in equilibrium with $CO_{(g)}$. In other words, the formation of COOH* is the potential-limiting step in CO_2 electroreduction to CO on Au and Ag and determines their activities. The electroreduction of CO* to CHO* or COH* determines the overpotential on Cu and other elements with stronger CO binding such as Ni.[33] Therefore, CO is expected to desorb at binding energies weaker than the energy of this equilibrium and, indeed, CO is the major product on these two metals, as measured experimentally.[34-38] If the CO_2 reduction is conducted in parallel to water reduction, it is possible to produce syngas ($CO + H_2$), which is, as mentioned before, an important feedstock for the chemical industry. Au and Ag can attend such requirement, however, for practical applications, the use of non-noble metal-based electrocatalysts would be desirable, and this is a difficult challenge in research.

Considering this scenario, in the present study, the CO_2 electrochemical reduction was investigated on different synthesized electrocatalysts. The reaction product distribution was probed via on line differential electrochemical mass spectrometer (DEMS) and quantitative faradaic efficiencies were carried out by means of in line gas chromatography aiming at identifying CO-selective electrocatalysts.

Experimental

Synthesis of carbon-supported nanoparticles

The synthesized electrocatalysts were formed by different metal nanoparticles supported on Vulcan carbon powder (XC-72R, ca. 20 nm and 220 $m^2\ g^{-1}$), and represented generically by metal/C. The considered eletrocatalysts in this study were Cu_2O-Cu/C, SnO_2/C, Cu_4Sn/C (4:1 nominal atomic ratio) alloy and Au/C and NiO/C (included for comparison). The Cu- and Au-based materials were synthesized by chemical reduction method.[39] Briefly, for Cu_2O-Cu/C and Cu_4Sn/C, 0.5 mmol of $CuCl_2.2H_2O$ (Sigma-Aldrich) was dissolved in a 250 mL sodium citrate solution (0.6 mmol) at room temperature, under nitrogen atmosphere and magnetic stirring. A Vulcan carbon slurry (1:1 water-isopropanol), previously prepared in an ultrasonic bath, was added and the mixture was sonicated to achieve a homogeneous state. This was followed by the addition of an aqueous sodium borohydride solution (13.2 mmol) (for Cu_4Sn/C, 0.12 mmol of $SnCl_2$ (Sigma-Aldrich) was also added at the same time) and the mixture was stirred for 4 h. The resulting black precipitates were filtered, washed with water and dried in an oven at

70 °C for 2 h. In order to increase the degree of alloying, the Cu_4Sn/C nanopowder was submitted to a heat treatment using a tubular oven (Maitec Materiais Industriais Técnicos) under argon atmosphere at 100 °C, for 1 h, and then reduced under a H_2 atmosphere at 500 °C for 3 h. The carbon-supported SnO_2/C and NiO/C nanoparticles (50 wt.% on carbon) were obtained by the impregnation method.[40,41] For which, 0.31 mmol $SnCl_2$, or $NiCl_2$, (Sigma-Aldrich) was dissolved in a 1:1 water-isopropanol suspension of Vulcan carbon, followed by sonication for 10 min, and by magnetic stirring at 80 °C in air, for the evaporation of the solvent and the consequent impregnation of the tin (or nickel) salt in the carbon powder. The impregnated carbon powder was submitted to a thermal treatment conducted in a muffle furnace (Fornitec) under air, at 400 °C for 3 h. The powder was washed with water and dried overnight at 70 °C.

Electrocatalyst characterization

Structural features and physical properties of the as-prepared materials were determined by X-ray diffraction (XRD) measurements, carried out using a Rigaku Ultima IV diffractometer with Cu Kα radiation, operating at 40 kV and 30 mA. The measured 2θ range was from 10 to 100º (with a scan rate of 1 degree min^{-1}). For Cu_4Sn/C, the metal atomic ratio was estimated by energy dispersive X-ray spectroscopy (EDS) analysis, using a Zeiss-Leica/LEO 440 model (LEO, UK) scanning electron microscopy (SEM) with a Link analytical micro-analyzer (Isis System Series 200). The distribution of the metal nanoparticles on the carbon powder support and the particle sizes were investigated by transmission electron microscopy (TEM) imaging, using a JEOL JEM2100 model microscopy, with a LaB_6 filament and operated at 200 kV accelerating voltage. The samples were prepared by dispersing the catalyst powders in an isopropyl alcohol solution using a sonicator for 10 min. After this, the suspended powders were loaded drop-wise on carbon-coated copper grids (Electron Microscopy Sciences) and dried under vacuum for 2 h.

The changes in the electronic/structural features of the Cu_4Sn/C and Cu_2O-Cu/C, electrocatalysts (under *in situ* conditions) were investigated by conducting X-ray absorption spectroscopy measurements (XAS) measurements in the X-ray absorption near edge structure (XANES) and X-ray absorption fine structure (XAFS) regions. The data were acquired in the transmission mode at the Cu K-edge (8979 eV), registered with reference to a metal copper foil during all measurements. The experiments were conducted at the D04-XAFS2 beam line of the Brazilian Synchrotron Light Laboratory (LNLS, Brazil), using a homemade spectro-electrochemical cell.[42,43] An 0.1 mol L^{-1} $KHCO_3$ aqueous electrolyte was confined in a chamber, and the thickness was externally adjusted for a maximized intensity of the transmitted X-ray beam. The working electrodes for the XAS measurements were prepared by mixing the electrocatalysts with Nafion® (ca. 30 wt.%) in isopropyl alcohol, followed by drying at ambient temperature. The Nafion-impregnated nanoparticle powders were sonicated for 10 min, followed by evaporation in air. The powders were then pressed at 25 °C and 3 ton for 1 min onto a disk-shaped carbon paper (Spectracorp, macroporous flow field, 30 wt.% wet, ca. 450 nm), resulting in a loading of 26 mg_{Cu} cm^{-2} (Cu_2O-Cu/C) or 20 mg_{Cu4Sn} cm^{-2} (Cu_4Sn/C). The counter electrode was a Pt screen cut in the center to allow the free passage of the X-ray beam. The *in situ* XAFS experiments were acquired during chronoamperometric measurements with the working electrodes polarized at different potentials in the range of the CO_2 electroreduction. All presented spectra were a result of the average of, at least, two independent measurements. The analysis of the XAS data was made by using the Athena package software.[44] The XANES spectrum, i.e., the absorption coefficient μ(E) *vs.* energy (E) curves, has been normalized, and spectra of different copper reference compounds (Cu_2O, CuO, $Cu(OH)_2$ and Cu foil) were obtained. In addition, the Fourier transformed spectrum was performed.

Differential electrochemical mass spectrometry (DEMS) experiments

The gaseous products derived from the CO_2 electroreduction were on line monitored via DEMS measurements.[45] DEMS equipment were constructed according to previous proposed setup, with a Pfeiffer Vacuum QMA 200 quadrupole mass spectrometer, and with two differentially pumped chambers, as described in details elsewhere.[46] This mass spectrometer setup allows on line and fast detection of volatile and/or gaseous species produced by electrochemical reactions during application of potential scans. In a typical DEMS experiment, therefore, the ionic current (mass signal intensity) *vs.* electrochemical potential curves are simultaneously recorded for selected values of mass/charge (*m/z*).[47-49] The homemade electrochemical cell, formed by three-neck round bottom flask (150 mL), and electrode/mass spectrometer interface (described below) were constructed based on a previous proposed setup in the literature.[50] The experiments were conducted in Ar- or CO_2-saturated 0.1 and 0.5 mol L^{-1} $KHCO_3$ electrolyte (Sigma-Aldrich), prepared using high purity water (Milli-Q, 18.2 MΩ cm) (pH solution of 8.5 and 6.8, respectively), with magnetic stirring (ca. 600 rpm). The potential was scanned in the range of –0.5 to –2.5 V (depending on the

experiment) with the scan rate of 1.0 or 10 mV s^{-1}, using an Autolab potentiostat (PGSTAT 30). The gaseous species hydrogen (H_2), methane (CH_4), ethylene (C_2H_4), carbon monoxide (CO) and dioxide carbon (CO_2) were individually monitored at the same time, at *m/z* 2, 15, 26, 28 and 44, respectively. The working electrodes, which are also the interface with the DEMS equipment, were composed by a disk-shaped carbon paper (Spectracorp™, macroporous flow field, 30 wt.% wet, ca. 450 mm, 12 mm diameter) bonded to a PTFE membrane (Gore-Tex® pore size 0.02 μm and 50 μm thick), previously prepared by pressing the carbon paper with the membrane at 1.0 ton cm^{-2}. For the electrocatalytic layer, a suspension of 4.0 mg mL^{-1} of the electrocatalyst was prepared by dispersing the studied powder in isopropyl alcohol, using an ultrasound bath, followed by dissolving 100 μL mL^{-1} of a Nafion 5% (DuPont) solution.[51] Thereafter, 300 μL aliquot of the dispersed suspension were pipetted onto a disk-shaped carbon electrode, and posteriorly to drying, the solvent at ambient air (90 μL of a diluted Nafion solution (0.01%)) was pipetted onto the surface in order to attach the nanoparticles on the carbon disk electrode.[51] After this step, the working electrode preparation was completed by positioning the carbon/Teflon disk onto the top of a stainless steel frit that mechanically supports the electrode. Finally, the electrical contact made by two were isolated from the electrolyte by using Teflon tape. So, it is wise to point here that there was no gold contact with the electrolyte solution. In addition to the nanoparticles, an electrode formed by sputtered gold and platinum layers on PTFE was also tested in order to compare the behavior of a CO-forming material (Au) with a selective H_2-forming material (Pt).[7] Also, the behavior of a Cu layer obtained by *in situ* electroredution of dissolved $CuSO_4$ salt (1.0 mmol L^{-1}, Merck) was also studied since Cu is one component of the Cu_4Sn/C nanoalloy material that is the central focus of the present investigation.[52]

For all electrochemical measurements, a platinum wire and a silver/silver chloride electrode (Ag/AgCl/Cl^-) were used as counter and reference electrodes, respectively. Cyclic voltammograms were recorded at 1 or 10 mV s^{-1}, and chronoamperometry were carried out at different potentials, depending on the experiment, according to the potential range for which the CO_2 reduction takes place.

Gas chromatography (GC)

The faradaic efficiency (FE) for CO on Cu_4Sn/C and Au/C was determined by using in line gas chromatograph (GC-2014, Shimadzu) during galvanostatic experiments.[53,54] The electrochemical cell was formed by compartments separated by a cation-exchange membrane (Nafion® 117). A platinum wire and a leak-free Ag/AgCl electrode (saturated KCl) were employed as counter and reference electrode, respectively, and the experiments were conducted in CO_2-saturated 0.1 mol L^{-1} $KHCO_3$ electrolyte. The working electrode was prepared in a similar manner that to for the DEMS measurements, but now depositing the electrocatalyst nanoparticles on three parallel arranged ribbon-shaped carbon papers (1 × 5 cm). The electrochemical experiments were conducted under galvanostatic conditions over ca. 800 s, after achieving stable values of electrochemical potentials.

The connection of the electrochemical cell cathodic compartment with the chromatograph was made by a stainless steel capillary (1/16'' outer diameter), onto which a flexible silicone-heating mantle was wrapped. The temperature was kept at 140 °C controlled by a temperature controller in order to avoid the condensation of water vapor or other eventual CO_2 reduction products. The capillary tube carried the gases into a regulating loop (200 μL) that allows automatic injection in the GC chromatograph. A Carboxen capillary GC column (Carboxen® 1010 PLOT, 30 m × 0.53 mm ID) was used for all experiments, and nitrogen as the mobile phase. A temperature ramp from 35 to 225 °C (10 °C min^{-1}) was programmed for allowing the desired separation of all the CO_2 reduction products, and the total required analysis time was 38 min. The GC chromatograph is equipped with a thermal conductivity detector (TCD) mainly for detecting H_2 and a flame ionization detector (FID) fitted with a methanizer for detecting CO and hydrocarbons. Both detectors were simultaneously used in order to maximize the detection signals. Standard gas mixture (1.0 atm, 298 K; CO, CO_2, C_2H_4 and C_2H_6 from White Martins) was used to calibrated the GC chromatograph for quantitative determination of the reaction products. During the galvanostatic conditions, and after ca. 800 s of the reduction reaction, a gas phase aliquot was injected into the GC chromatograph by the automatic sampler. Blank measurements using Ar-saturated electrolyte with and without polarization, and CO_2-saturated electrolyte, without polarization were also recorded. The experimental data was collected and translated to faradaic efficiencies considering standard conditions and calculated by equation 6:

$$\text{FE (product CO)} = \frac{e_{output}}{e_{input}} \times 100 \quad (6)$$

where e_{output} is the number of mols of electrons required for reducing CO_2 to CO (recorded amount of product in mol × number of electrons required to obtain one molecule of the product); e_{input} is the total number of mols of electrons

measured during the galvanostatic period, obtained from equation 7:

$$e_{input} = (I \times t)/F \quad (7)$$

where I is the recorded current in ampere (A), F the Faraday constant (96485 C mol^{-1}) and t the time required to fill the sampling loop in seconds considering the flow rate of CO_2. The recorded amount of the CO product (mol) was obtained from each chromatogram peak area in comparison of the standard gas mixture, measured before each individual experiment.

Results and Discussion

The crystallite structures and the particle distribution on the Vulcan carbon support of Cu_2O-Cu/C, SnO_2/C, Au/C, NiO/C and Cu_4Sn/C were investigated by XRD and TEM. The obtained XRD patterns, presented in Figure 1, evidences major phases of SnO_2, Cu_2O, and NiO for the SnO_2/C, Cu_2O-Cu/C and NiO/C eletrocatatalysts. For Au/C, as expected, the diffraction patterns indicate the metallic phase with the face-centered cubic structure. The diffraction peaks for Cu_4Sn/C nanoparticle clearly show a totally different diffraction pattern from that of pure copper or pure tin due to alloy formation, generating the Cu_4Sn phase.[55-58] The obtained average crystallite sizes for SnO_2/C and NiO/C were 5.6 and 4.0 nm, respectively, and for Cu_2O-Cu/C, Cu_4Sn/C and Au/C, the values were of 15.7, 32 and 16 nm, respectively. Figures 2a-2e show the representative bright-field (BF)-TEM images for the as-synthesized electrocatalysts. The images reveal different particles sizes, depending on the electrocatalyst, in accordance with the different crystallite sizes as obtained from XRD. For SnO_2/C and NiO/C (SnO_2 and NiO phases), presented in Figures 2a and 2e, the TEM images reveal homogeneous distribution of the particles on the support, but, due to their low contrast with the Vulcan carbon, their sizes could not be precisely determined. For the Cu_4Sn/C alloy (Figure 2c), the results evidence the presence of individual particles and particle agglomeration. Contrarily, the TEM image for Au/C (Figure 2d) shows a homogeneous distribution of the gold nanoparticles on the carbon support, with most of the nanoparticles with sizes varying in range of 2.3-4.7 nm, and with few bigger particles in the range of 9.5-18 nm. The lower values of crystallite or particle sizes for SnO_2/C and NiO/C are due to the formation of SnO_2 and NiO nanoparticles, instead of metallic tin or nickel, this being a consequence of the utilized synthesis route (impregnation followed by thermal treatment in air). Cu_2O-Cu/C and Cu_4Sn/C were obtained via chemical reduction of their ion solution, in the presence of the carbon support, and this may conduct to higher sizes. The much higher average crystallite size for Cu_4Sn/C is attributed to the thermal treatment at 400 °C in H_2 atmosphere in order to induce alloy formation. Au/C was synthesized via chemical reduction in solution, with colloidal suspension formation (in the absence of the support in suspension). Particularly for the case of Au/C, this method results in nanoparticles with few nanometers.[59] But, for high loadings on carbon powder, that is the case of this study (50 wt.%), larger particles (higher than 10 nm) are expected. Nevertheless, these differences will not influence the product distribution comparison or the quantitative determination of the faradaic efficiencies, investigated by on line DEMS and in line GC that will be presented in the next sections.

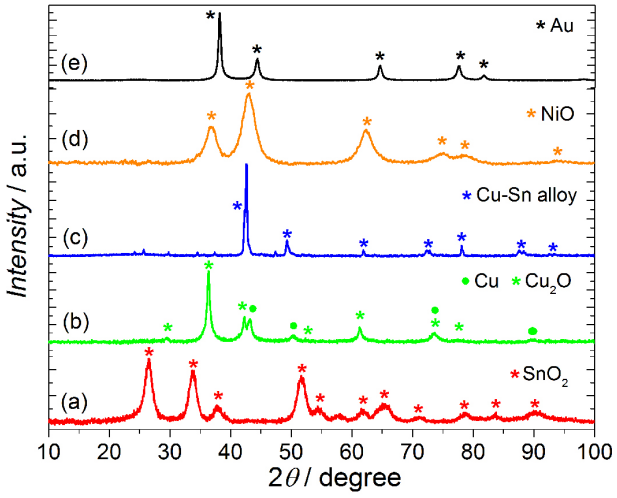

Figure 1. X-Ray powder diffraction intensities for the synthesized nanoparticles: (a) SnO_2/C, (b) Cu_2O-Cu/C, (c) Cu_4Sn/C, (d) NiO/C and (e) Au/C. The positions of the diffraction peaks of the reference materials were included for comparison.

The investigation of the copper reactivity or structural/oxidation state changes as a function of the applied potential for the Cu_2O-Cu/C and Cu_4Sn/C electrocatalysts measured via *in situ* XAS experiments in the Cu K-edge is presented in Figure 3. The *in situ* XANES results for Cu_2O-Cu/C (Figure 3a) (the spectra obtained for the CuO, Cu_2O, $Cu(OH)_2$ reference oxides and for a metallic copper foil were included for comparison) clearly evidence that at open-circuit condition, the spectrum resembles that of Cu_2O. By decreasing the electrochemical potential from OCP (open circuit electrode potential) to –1.5 V, it is noticeable the gradual transformation of the Cu_2O phase, being, ultimately, converted to metallic copper at –2.0 V (resembling the XANES spectrum of the metallic copper foil). This conversion can also be observed in the plot of the Fourier transform of the EXAFS (extended X-ray absorption

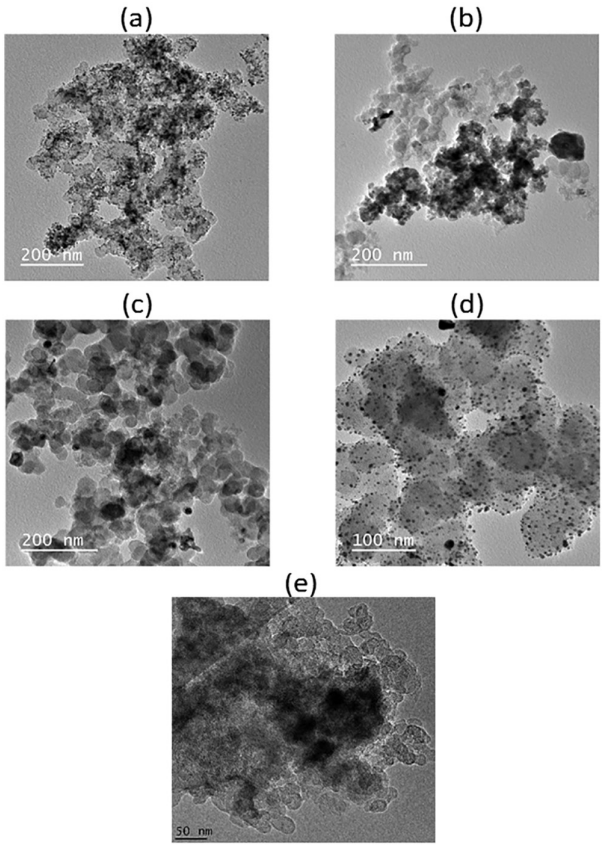

Figure 2. TEM images of the different carbon-supported nanoparticles: (a) SnO_2/C, (b) Cu_2O-Cu/C, (c) Cu_4Sn/C, (d) Au/C and (e) NiO/C.

fine structure) oscillations, presented in Figure 3b, in which the peak ascribed to Cu–O is converted to the Cu–Cu coordination. Therefore, it means that the as-prepared Cu_2O-Cu/C electrocatalyst (initially formed by Cu_2O (major phase)) suffers *in situ* transformation to metallic copper in the potential domain that the CO_2 electroreduction takes place. The XANES spectra for Cu_4Sn/C (Figure 3c) show only some changes in the spectrum profile as a function of the potential, but these changes can be better evidenced by Fourier transform of the EXAFS oscillations (Figure 3d). The peak associated to Cu–O (at ca. 1.5 Å, with low intensity) and the peak ascribed to the Cu–Cu coordination (at ca. 2.2 Å) are observed. Interestingly, the Cu–Cu coordination of the Cu_4Sn/C material is located at a slightly higher value of R (variable proportional to the interatomic distance), compared to the Cu–Cu peak of the Cu foil, indicating that the Cu–Cu interatomic distance suffered a tensile strain. This is consistent with the insertion of the Sn atoms (larger atomic radii) into the Cu structure. By decreasing the electrochemical potential, the peak related to Cu–O decreases in intensity, with a concomitant increase in the intensity of the peak for the Cu–Cu coordination (mainly seen at –2.0 V). Hence, this would suggest that, initially, the Cu_4Sn/C electrocatalyst is covered by oxide/hydroxide species and, by decreasing the electrochemical potential down to –1.5 V, and, more severely, to –2.0 V, these species are stripped off from the surface, yielding Cu and Sn atoms in their metallic states. Despite the fact of been synthesized by a different manner, Sarfraz *et al.*[60] by using Auger electron spectroscopy also evidenced the existence of metallic Cu and Sn on Cu–Sn alloys after the electrocatalytic reaction (low potentials).

Electrochemical experiments

Electrocatalytic reduction of CO_2 investigated by on line DEMS

The ionic current for *m/z* 28 can be employed for monitoring the CO formation. However, the *m/z* 28 signal combines the contribution from the CO molecules produced from CO_2 electroreduction with that of CO species originated from the CO_2 fragmentation (that is present in the saturated electrolyte) in the mass spectrometer. According to the literature,[24] gold has medium HER overvoltage, and possess weak CO adsorption, which justify its known high CO production selectivity during the CO_2 electroreduction. Platinum, on the other hand, has low HER overpotential and strong CO adsorption. In aqueous media, the CO_2 electroreduction does not take place on platinum, only the hydrogen evolution from water electroreduction occurs, with 100% of faradaic efficiency. Considering this scenario, firstly, the DEMS experiments for the electroreduction of CO_2 were explored for Au/PTFE and Pt/PTFE electrodes (sputtered metal on porous Teflon membrane) in order observe the behavior of the *m/z* 28 ionic current, and check if CO could be detected, separated from the contribution from CO_2, for CO-forming electrocatalysts. Figure 4 shows the faradaic and ionic currents for *m/z* 2 (H_2), 28 (CO) and 44 (CO_2) obtained during DEMS experiments of cyclic voltammetry for the Au/PTFE and Pt/PTFE electrodes in CO_2-saturated 0.5 mol L^{-1} $KHCO_3$ aqueous electrolyte at 25 °C . For both Pt/PTFE and Au/PTFE, H_2 produced by the hydrogen evolution reaction (water electroredution) is detected with much lower overpotential for Pt/PTFE. At higher overpotentials, the very large production of H_2 saturates the mass spectrometer detector, and the signal forms a plateau. For Pt/PTFE, as CO is not produced via CO_2 electroreduction, this increase in the H_2 signal is accompanied by a decrease of the mass-to-charge 28 (Figure 4c) due to the depletion of dissolved CO_2 in the vicinities of the electrode (the H_2 production vanishes the local CO_2). For Au/PTFE electrode, on the other hand, even with parallel H_2 generation via water electroreduction, as CO is produced, the increase

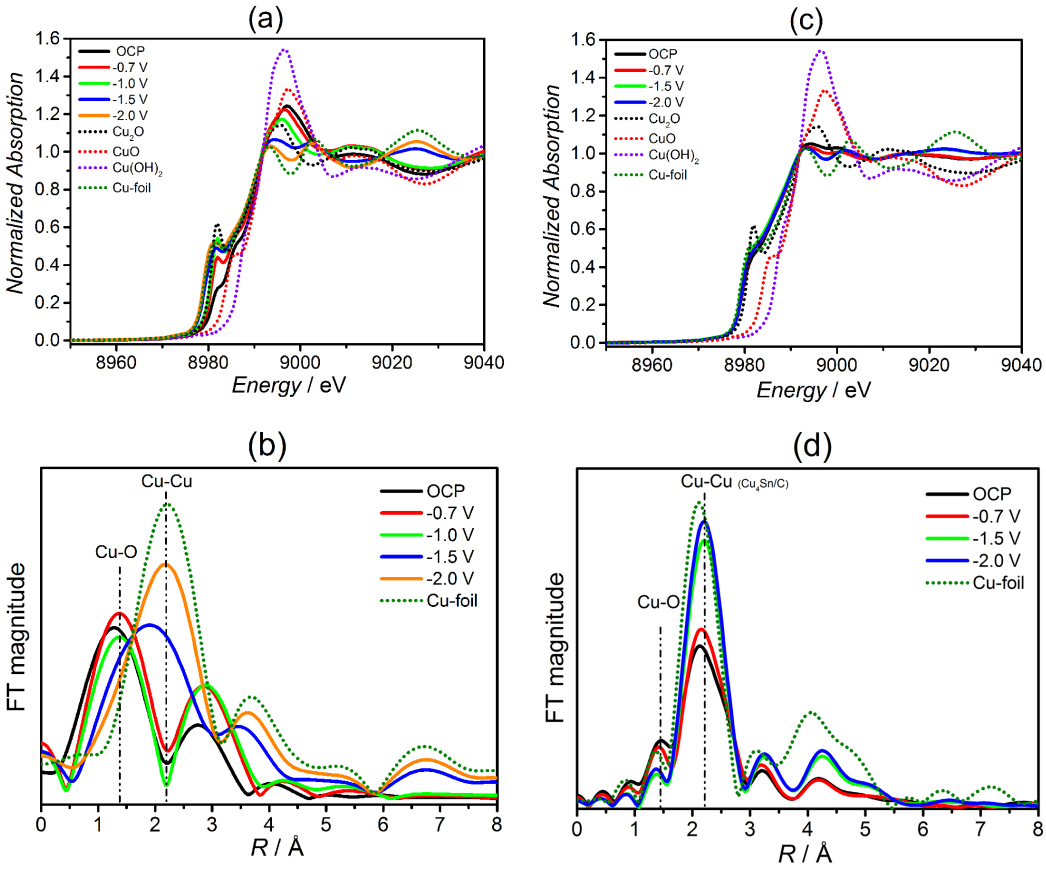

Figure 3. *In situ* XANES spectra at the Cu K-edge and Fourier transform (k^3 weighted) of the EXAFS oscillations for Cu_2O-Cu/C ((a) and (b)) and for Cu_4Sn/C ((c) and (d)), respectively, obtained during electrochemical polarization at different potentials. The spectra of reference samples of Cu_2O, CuO, $Cu(OH)_2$ and Cu foil (obtained *ex situ*) were included for comparison.

in the *m/z* 28 ionic current, related to CO, becomes evident. This trend was also investigated for the case of nanoparticles. Figure 5 shows the faradaic and the ionic currents obtained during DEMS experiments of cyclic voltammetry in CO_2-saturated electrolyte for Au/C, a CO-producing material, and for NiO/C nanoparticles, a known electrocatalyst that produces only H_2 during the CO_2 electrochemical reduction in aqueous media. As can be seen, the ionic signal for H_2 (Figure 5b) increases concomitantly with the faradaic current (Figure 5a), and the current for *m/z* 28 (Figure 5c) drops due to the CO_2 depletion in the electrolyte in the vicinities of the electrode surface. However, for Au/C, the *m/z* 28 signal increases attributable to the formation of CO, even with the negative contribution of CO_2 for the *m/z* 28 ionic current, due to its depletion. Therefore, these results indicate that CO can be detected by DEMS using the *m/z* 28 ionic current for CO-forming electrocatalysts, even with the influence of the CO_2 fragmentation to the *m/z* 28 signal. Few other articles have studied the CO production by on line mass spectrometry, separating it from the CO_2 contribution, for qualitative comparison of different electrocatalysts.[61,62] As it will be discussed below, for copper (unique pure metal that produces methane and ethylene), the *m/z* 28 ionic current cannot be used for monitoring CO because these molecule fragmentations also contribute to this signal.

Seeing that copper is the major component of the Cu_4Sn/C alloy, its behavior was studied firstly. It is reported in literature that copper catalyzes the production of methane and ethylene in addition to hydrogen, during the CO_2 electroreduction.[63-66] Here, it was studied the behavior of electrodeposited copper, performed with *in situ* electrodeposition of Cu^{2+} ions on the Au/PTFE electrode (adding 2.0 mmol L^{-1} $CuSO_4$ salt in the CO_2-saturated 0.1 mol L^{-1} $KHCO_3$ electrolyte). Figure 6 presents the faradaic and ionic signals for *m/z* 2 (H_2), 15 (CH_4) and 26 (C_2H_4) (a) *vs.* electrochemical potential and (b) *vs.* time obtained during DEMS experiments of cyclic voltammetry in CO_2-saturated $KHCO_3$ electrolyte. The 1st and the 2nd cycles were conducted in the absence of Cu^{2+} in solution and the ionic currents show that H_2 is the unique reaction production (CO, not measured here). This is produced by the sputtered gold layer substrate (the small peaks for *m/z* 15 and 26 are due to the variation of the baseline, due to the influence of the hydrogen formation, which alters the partial pressures in the DEMS main chamber). Posterior to the 2nd cycle, $CuSO_4$ was

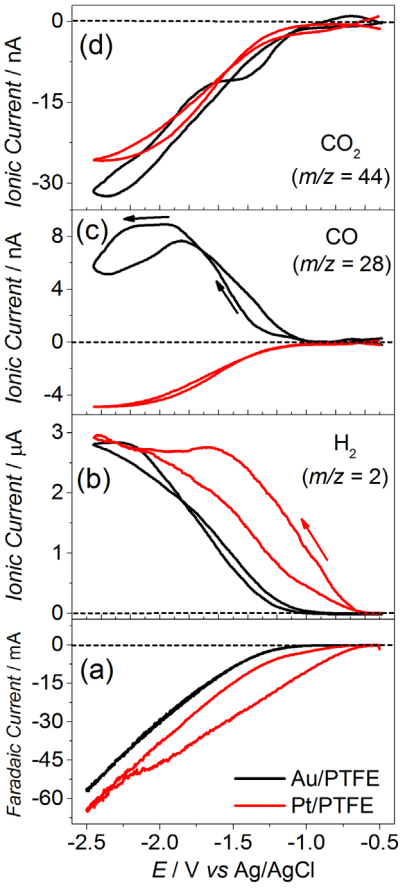

Figure 4. Faradaic and ionic currents for *m/z* 2 (H_2), 28 (CO) and 44 (CO_2) obtained during DEMS experiments of cyclic voltammetry (10 mV s^{-1}) for the Au/PTFE (black curve) and Pt/PTFE (red curve) electrodes in CO_2-saturated (line) and Ar-saturated (dot) 0.5 mol L^{-1} $KHCO_3$ electrolyte at 25 °C.

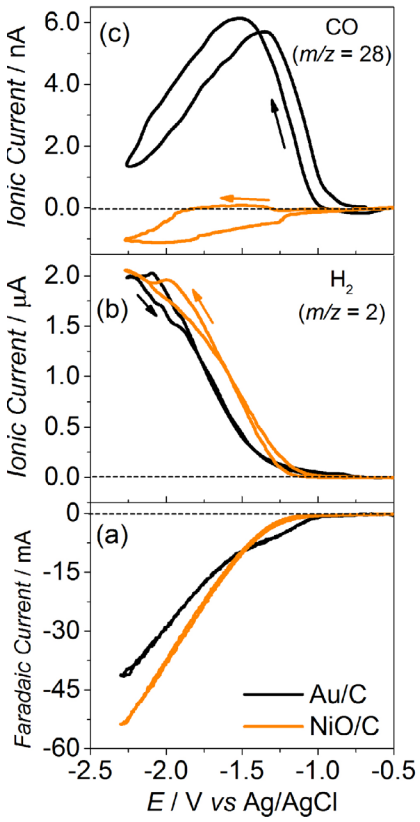

Figure 5. Faradaic and ionic currents for *m/z* 2 (H_2) and 28 (CO) obtained during DEMS experiments of cyclic voltammetry (1.0 mV s^{-1}) in CO_2-saturated 0.5 mol L^{-1} $KHCO_3$ electrolyte at 25 °C for the different investigated electrocatalysts.

rapidly added to the electrolyte and, after potential excursion to low values (3rd cycle), copper is electrodeposited on the Au/PTFE and, subsequently, methane and ethylene start to be detected. Methane reaches its maximum in the consecutive cycle, suffering an accentuated decrease afterwards. The signal for ethylene increases until the 6th cycle and, after that, seems to define a plateau. However, previous data reported in the literature[63] show that the ethylene signal also drops with time, but the rate of its decrease is less accentuated than that of methane. Such deactivation, however, is not clear comprehended, but it seems to be related to the formation of irreversible or inert adsorbed carbonaceous species (graphite-like) on the copper surface,[63,67] or due to the formation of copper carbonate hydroxide (copper oxide patina) during the course of the CO_2 electroreduction in the aqueous electrolyte.[68]

The DEMS measurements obtained during cyclic voltammetry experiments at 1.0 mV s^{-1} for CO_2 electroreduction, catalyzed by the synthesized Cu_4Sn/C alloy and by the Cu_2O-Cu/C and SnO_2/C nanoparticles (the alloy components), are shown in Figure 7. For Cu_2O-Cu/C, only the first voltammetric cycle is presented, since, as presented above, it suffers severe deactivation during the CO_2 electroreduction. For the other two materials, their faradaic and ionic currents were quite stable upon cycling, as discussed below. It is noted that the faradaic current is higher for Cu_2O-Cu/C and very similar for SnO_2/C and Cu_4Sn/C (Figure 7a), while the ionic signals for CO and H_2 formation present different distribution. SnO_2/C has low H_2 production (metal with high hydrogen overpotential), and catalyzes the CO_2 electrochemical reduction to CO (Figure 7e). Actually, previously published works have found that, even at negative potentials, tin may exist as tin hydroxide[69] and the main product of the CO_2 electroreduction is formate ions,[14] being CO a parallel or secondary product (formate cannot be detected be DEMS). So, part of the electrochemical current for SnO_2/C observed in Figure 7a is spent in the production of formate ions, which is not counted in the present study, explaining the lowest ionic currents for CO and H_2. For Cu_2O-Cu/C, all the measured ionic signals are higher than those of the other two electrocatalysts, being consistent with its higher faradaic current. As presented above,

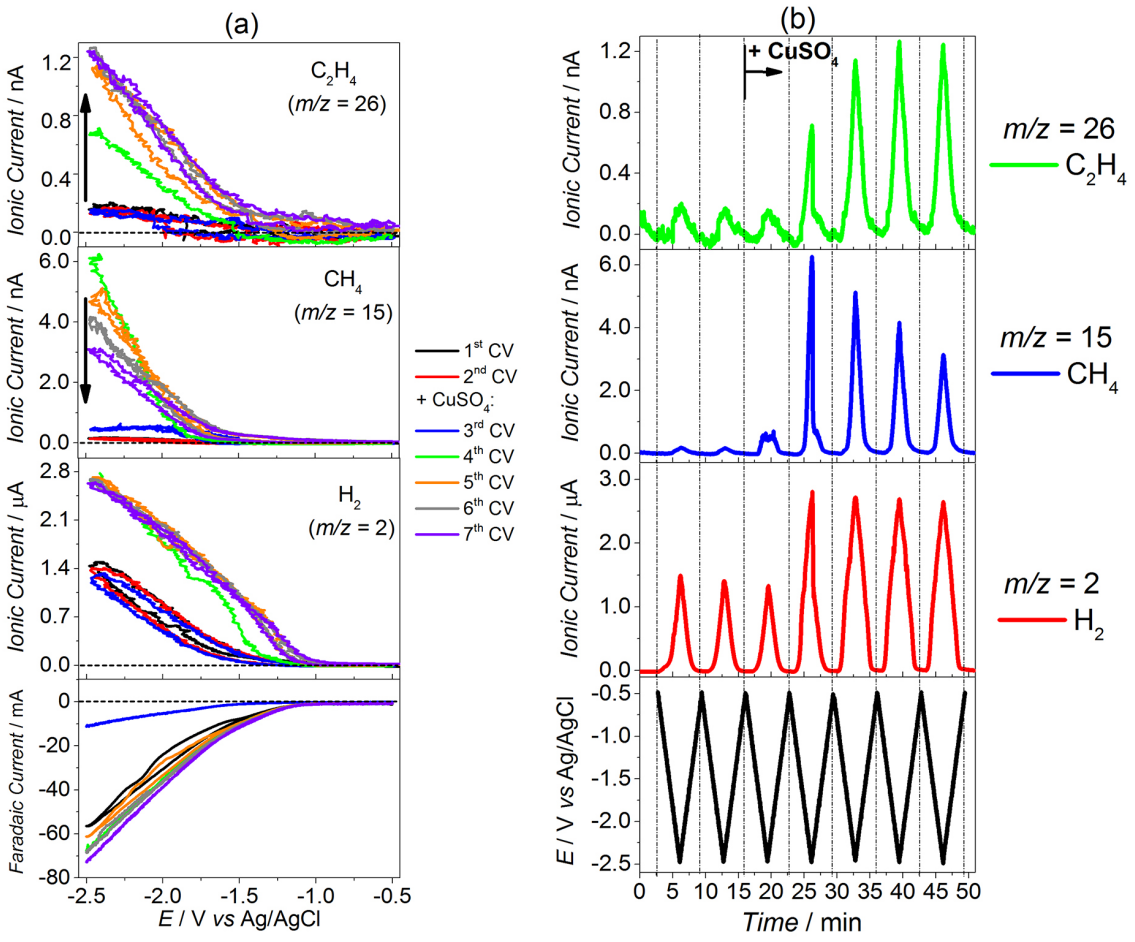

Figure 6. Faradaic and ionic currents for *m/z* 2 (H_2), 15 (CH_4) and 26 (C_2H_4) obtained during DEMS experiments of cyclic voltammetry (10 mV s^{-1}) for the Au/PTFE electrode in CO_2-saturated 0.1 mol L^{-1} $KHCO_3$ electrolyte at 25 °C: (a) *vs.* potential and (b) *vs.* time after the 3rd CV scan ($CuSO_4$ (to reach 1.0 mmol L^{-1}) was added to the electrolyte).

copper produces methane and ethylene (according to the literature, the faradaic efficiencies are 33.3 and 25.5%, respectively)[58,60,70] and, since fragmentation of these molecules yields *m/z* 28, both contribute to this ionic current in the DEMS measurements. Therefore, the higher *m/z* 28 signal observed for Cu_2O-Cu/C (Figure 7e) is ascribed, predominantly, to the formation of methane and ethylene. Curiously, Cu_4Sn/C and SnO_2/C possess similar ionic currents for H_2, but Cu_4Sn/C shows higher ionic current for CO formation. It is worth mentioning that methane (*m/z* 15) and ethylene (*m/z* 26) were not detected during the CO_2 electroreduction catalyzed by Cu_4Sn/C and/or SnO_2/C, as can be observed in Figures 7c and 7d. The slight variation on their ionic currents are, actually, due to the variation of their baselines, induced by the hydrogen gas that is produced during the very negative polarizations. So, all the ionic currents for *m/z* 28 for Cu_4Sn/C and/or SnO_2/C are ascribed to the CO production.

As long as Cu_4Sn/C was identified as the electrocatalyst with the larger CO generation, its efficiency was determined via experiments of in line chromatography. For comparison, the experiments were also conducted, at the same conditions, for Au/C, a known electrocatalyst for selective CO_2 electroreduction to CO. The faradaic efficiencies for CO formation, obtained during galvanostatic experiments at ca. 10 mA cm^{-2} (ca. –1.5 V) for the CO_2 electrochemical reduction, resulted in 13 and 23% for Cu_4Sn/C and Au/C, respectively. In addition to the determination of the faradaic efficiencies, the stability of Au/C and Cu_4Sn/C for the CO_2 electrochemical reduction was studied. Figures 8a and 8b present the imposed electrochemical potential and ionic currents for *m/z* 28 (CO) and for *m/z* 2 (H_2), as a function of time for Au/C and Cu_4Sn/C, respectively, obtained during chronoamperometric experiments for CO_2 electroreduction. It is noted that the potential step from OCP to –1.3 V for Au/C induces a step in the ionic currents due to the H_2 and CO formation. However, the CO signal (*m/z* 28) undergoes a significant decrease as a function of time, with the concomitant increase in the signal for H_2 formation (*m/z* 2). This means that the route of CO formation is

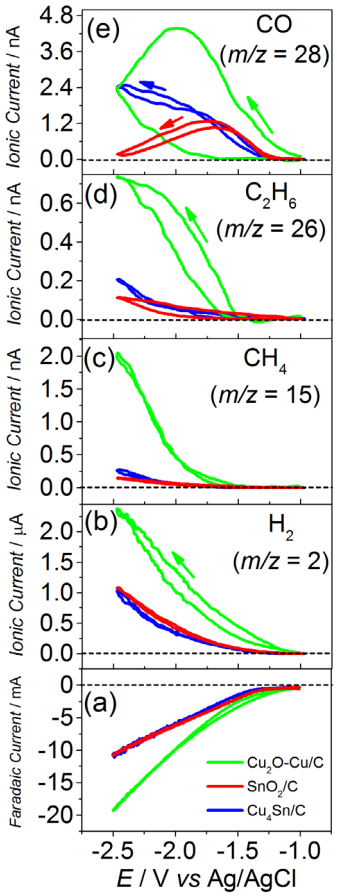

Figure 7. Faradaic and ionic currents for *m/z* 2 (H_2), 15 (CH_4), 26 (C_2H_4) and 28 (CO) obtained during DEMS experiments of cyclic voltammetry (1.0 mV s^{-1}) in CO_2-saturated 0.1 mol L^{-1} $KHCO_3$ electrolyte at 25 °C for the different investigated electrocatalysts.

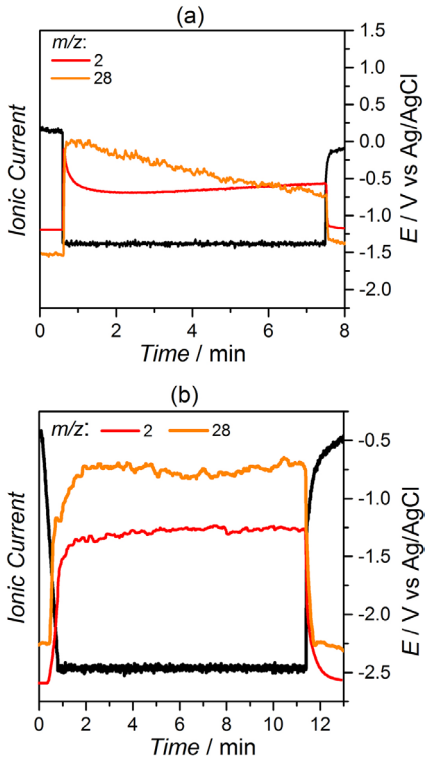

Figure 8. Ionic currents for *m/z* 2 (H_2) and 28 (CO) as a function of the time obtained during DEMS measurements of chronoamperometry in CO_2-saturated 0.1 mol L^{-1} $KHCO_3$ electrolyte at 25 °C for: (a) Au/C and (b) Cu_4Sn/C (the imposed electrochemical potential is also included in black line).

inhibited (or blocked) and the electrons are used to reduce water. It was experimentally observed that the CO signal is restored to its initial value only after potential excursion to higher potential (close to 1.0 V), but the subsequent polarization at negative values for CO_2 reduction leads to the same signal behavior of deactivation. This deactivation or poisoning of gold during the CO_2 electroreduction to CO was also observed by Kedzierzawski *et al.*[71] Based on the results of cyclic voltammetry, conducted after experiments of polarization for CO_2 electroreduction, they stated that adsorbed CO is not the cause of the observed deactivation of the gold electrode. Some other adsorbed reaction intermediate, that suffers electrochemical oxidation at potentials higher than that for CO, is likely to be the reason for such observed deactivation. However, additional experiments, including *in situ* techniques, are necessary to identify this poisoning species. Contrarily to Au/C, the chronoamperometric curves for CO_2 electroreduction on Cu_4Sn/C presented a stable behavior, with constant rates of CO and H_2 formation, as evidenced by the ionic currents for *m/z* 28 and 2 (Figure 8b).

Although the Cu_4Sn/C electrocatalyst presented lower faradaic efficiency than that of Au/C, the magnitudes are comparable and, so, the obtained result is stimulating considering that this electrocatalyst is formed by non-noble metals. Clearly, a synergistic effect is observable for Cu_4Sn/C in view of the higher CO production when compared to that of the individual metals that form the alloy, as evidenced by the on line DEMS experiments.

The change in the product selectivity as a consequence of alloying Cu and Sn was also observed in a previous work.[60] The main point is to understand how the active site is modified between pure Cu (or pure Sn) and Cu-Sn alloy, which makes the electrocatalyst more selective toward CO. Hansen *et al.*[33] proposed different steps for the CO_2 electroreduction reaction, for which, firstly, the CO_2 is reduced forming an adsorbed COOH (*COOH) specie, and this is followed by an additional reduction producing adsorbed CO and H_2O (equations 8 and 9). For metals that present weak binding energy for CO, such as Au and Ag, this species simply desorb from the electrode, resulting in high faradaic efficiencies for CO production. For Au and Ag, the formation of COOH* is the limiting step and determines their activities for reduction of CO_2 to CO. The additional reduction of CO to CHO* species

(equation 10) requires further steps of hydrogen addition, and this is possible on metals with intermediate and strong binding of CO, such as Cu and Pd.

$$CO_2 + * + e^- + H^+ \rightarrow COOH* \quad (8)$$
$$COOH* + e^- + H^+ \rightarrow CO* + H_2O \quad (9)$$
$$CO* + e^- + H^+ \rightarrow CHO* \quad (10)$$

A previous study of Sarfraz *et al.*[60] (by density functional theory (DFT) calculations) evidenced that the substitution of a Cu atom by a Sn atom does not cause changes in the d-band structure. Consequently, the increased CO production brought by alloying Cu and Sn, in relation to that of these pure metals, would not be attributed to changes in the CO binding energy due to electronic changes. Indeed, according to recent results of Hansen *et al.*,[33] intermetallic compounds of Au, Ag and Cu with elements such as Sn, Zn, Ga and In are active for CO_2 electroreduction to CO, and this was ascribed to the stabilization of the COOH* intermediate, relative to the CO* intermediate, due to the enhanced interaction with the O end of the COOH* with the oxophilic element. Thus, as the principal reason, the observed increase in the CO production on Cu_4Sn/C is due to the composition or structural effect, being associated to the role of the Sn atoms inserted on the Cu structure or in intimate contact with the Cu atoms. In fact, when the CO_2 electroreduction was conducted on electrodes obtained by electrodepositing copper and tin, simultaneously (not shown here for brevity), without alloy formation, the generated products were the sum of those formed on copper and on tin, individually (no synergistic effect). So, it seems the tin atoms must be present in close contact with copper in order to achieve this intermediate stabilization effect. It is reasonable to argue, therefore, that the COOH* species may be stabilized due to the oxygen interaction with the oxophilic Sn atoms in the vicinities of Cu, so, accelerating its formation, letting CO free for desorption in the consecutive step. Sarfraz *et al.*[60] considered that the Sn atoms in the Cu–Sn alloys lead to the suppression of the catalytic activity for H_2 evolution without affecting the productivity toward CO. Really, the on line DEMS experiments (Figure 7b) have showed that the incorporation of Sn on Cu reduced HER in comparison to that of pure Cu_2O-Cu/C nanoparticles. This would be related to the weaker adsorption of hydrogen on Cu_4Sn/C, compared to that of pure Cu, which leads to lower H coverage degree, resulting in a decreased H_2 evolution. So, the lowered HER would intensify the carbon dioxide electroreduction pathway. Also, the Sn-modified Cu nanoparticle surface may also hinder or decelerate the proton addition (protons originated from water) in the subsequent steps of CO electroreduction (CO* → CHO*, and further consecutive steps), and this is indirectly observed in the DEMS results for Cu_4Sn/C (Figures 7c and 7d), that show the suppression or reduction of the methane and ethylene signals in relation to those for Cu_2O-Cu/C. Although the obtained results still show low faradaic efficiency for CO production, mainly due to the competitive water electroreduction (HER), it is expected that these studies in aqueous media, determining selective electrocatalysts, help as a guide or inspiration for the development of more efficient CO_2 electrolyzers, even for those working with organic or hybrid organic/aqueous electrolytes.[72]

Conclusions

The results obtained herein showed that the CO formation can be monitored by using a modified electrode and electrochemical cell, on line coupled to a differential electrochemical mass spectrometer. The on line DEMS data showed that the Cu_4Sn/C alloy nanoparticle produces CO with an amount that can be comparable to that of Au/C, a known electrocatalyst with high activity for CO_2 electroreduction to CO. The DEMS measurements also evidenced that the introduction of Sn atoms on Cu suppress the methane and ethylene production, and diminish the hydrogen evolution reaction in relation to that on pure Cu_2O-Cu/C. Quantitative results, obtained via in line gas chromatography experiments, have evidenced faradaic efficiencies for CO formation of 13 and 23% for Cu_4Sn/C and Au/C, respectively. The *in situ* XAS experiments, obtained during potentiostatic polarizations in the CO_2 reduction potential domain, showed that the Cu_4Sn/C material presents significant structure/composition stability. Additionally, the DEMS measurements showed stable faradaic and ionic currents for CO formation on this electrocatalyst. Au/C, on the contrary, showed progressive deactivation, and this was ascribed to the poisoning of reaction intermediates that are stripped off only after potential excursions to higher potentials. The selectivity of Cu_4Sn/C for the CO_2 electroreduction to CO was ascribed to the Sn role and on (*i*) stabilizing the adsorbed HCOO intermediate specie, that is the precursor for the CO formation; and (*ii*) on decreasing the HER. This conducts to the deviation from the pathway of further hydrogenation of adsorbed intermediates, avoiding the transformation to adsorbed CHO, that is the precursor for the methane and ethylene formation and, so, letting CO free for desorption. Therefore, it is shown here that stable electrocatalytic reduction of CO_2 to CO can be achieved by using a non-noble metal alloy electrocatalyst, and a fine-tuning of the composition and/or structure may increase the faradaic

efficiency. It is expected that these results can be used as a guide for further development of electrocatalysts, even for non-aqueous electrolytes.

Acknowledgments

The authors gratefully acknowledge financial support from FAPESP (Fundação de Amparo à Pesquisa do Estado de São Paulo, F. H. B. L. grant No. 2016/13323-0 and 2013/16930-7 and M. R. C. grant No. 2014/26699-3), CNPq (Conselho Nacional de Desenvolvimento Científico e Tecnológico, F. H. B. L. grant Nos. 477153/2013-5, 306213/2013-3, and 306469/2016-2), FAPEMA (Fundação de Amparo à Pesquisa do Estado do Maranhão, W. O. S. grant No. BD-01638/13), and Brazilian Synchrotron Light Laboratory (LNLS, XAFS2 beam line) for assisting with the XAS experiments.

References

1. Kondratenko, E. V.; Mul, G.; Baltrusaitis, J.; Larrazábal, G. O.; Pérez-Ramírez, J.; *Energy Environ. Sci.* **2013**, *6*, 3112.
2. Pacala, S.; Socolow, R.; *Science* **2004**, *305*, 968.
3. Song, C.; *Catal. Today* **2006**, *115*, 2.
4. Aresta, M. In *Carbon Dioxide as Chemical Feedstock*; Aresta, M., ed.; Wiley-VCH Verlag GmbH & Co. KGaA: Weinheim, Germany, 2010.
5. Windle, C. D.; Perutz, R. N.; *Coord. Chem. Rev.* **2012**, *256*, 2562.
6. Tatin, A.; Comminges, C.; Kokoh, B.; Costentin, C.; Robert, M.; Savéant, J. M.; *Proc. Natl. Acad. Sci. U. S. A.* **2016**, *113*, 5526.
7. Hori, Y.; Wakebe, H.; Tsukamoto, T.; Koga, O.; *Electrochim. Acta* **1994**, *39*, 1833.
8. Delacourt, C.; Ridgway, P. L.; Kerr, J. B.; Newman, J.; *J. Electrochem. Soc.* **2008**, *155*, B42.
9. Yamamoto, T.; Tryk, D. A.; Fujishima, A.; Ohata, H.; *Electrochim. Acta* **2002**, *47*, 3327.
10. Choudhary, V. R.; Uphade, B. S.; Belhekar, A. A.; *J. Catal.* **1996**, *163*, 312.
11. Jitaru, M.; *J. Univ. Chem. Technol. Metall.* **2007**, *42*, 333.
12. Kumar, B.; Brian, J. P.; Atla, V.; Kumari, S.; Bertram, K. A.; White, R. T.; Spurgeon, J. M.; *Catal. Today* **2016**, *270*, 19.
13. Sreekanth, N.; Phani, K. L.; *Chem. Commun.* **2014**, *50*, 11143.
14. Chen, Y.; Li, C. W.; Kanan, M. W.; *J. Am. Chem. Soc.* **2012**, *134*, 19969.
15. Hansen, H. A.; Varley, J. B.; Peterson, A. A.; Nørskov, J. K.; *J. Phys. Chem. Lett.* **2013**, *4*, 388.
16. Li, C. W.; Kanan, M. W.; *J. Am. Chem. Soc.* **2012**, *134*, 7231.
17. Baturina, O. A.; Lu, Q.; Padilla, M. A.; Xin, L.; Li, W.; Serov, A.; Artyushkova, K.; Atanassov, P.; Xu, F.; Epshteyn, A.; Brintlinger, T.; Schuette, M.; Collins, G. E.; *ACS Catal.* **2014**, *4*, 3682.
18. Ren, D.; Deng, Y.; Handoko, A. D.; Chen, C. S.; Malkhandi, S.; Yeo, B. S.; *ACS Catal.* **2015**, *5*, 2814.
19. Varela, A. S.; Kroschel, M.; Reier, T.; Strasser, P.; *Catal. Today* **2016**, *260*, 8.
20. Zhang, S.; Kang, P.; Meyer, T. J.; *J. Am. Chem. Soc.* **2014**, *136*, 1734.
21. Liu, Z.; Masel, R. I.; Chen, Q.; Kutz, R.; Yang, H.; Lewinski, K.; Kaplun, M.; Luopa, S.; Lutz, D. R.; *J. CO_2 Util.* **2016**, *15*, 50.
22. Ma, M.; Trześniewski, B. J.; Xie, J.; Smith, W. A.; *Angew. Chem., Int. Ed.* **2016**, *55*, 9748.
23. Koga, O.; Hori, Y.; *Electrochim. Acta* **1993**, *38*, 1391.
24. Li, W. In *Advances in CO_2 Conversion and Utilization*, *ACS Symposium Series*, vol. 1056; American Chemical Society: Houghton, MI, USA, 2010, p. 55.
25. Hirunsit, P.; Soodsawang, W.; Limtrakul, J.; *J. Phys. Chem. C* **2015**, *119*, 8238.
26. Shibata, H.; Moulijn, J. A.; Mul, G.; *Catal. Letters* **2008**, *123*, 186.
27. Qiao, J.; Liu, Y.; Hong, F.; Zhang, J.; *Chem. Soc. Rev.* **2014**, *43*, 631.
28. Hori, Y.; Konishi, H.; Futamura, T.; Murata, A.; Koga, O.; Sakurai, H.; Oguma, K.; *Electrochim. Acta* **2005**, *50*, 5354.
29. Kortlever, R.; Shen, J.; Schouten, K. J. P.; Calle-Vallejo, F.; Koper, M. T. M.; *J. Phys. Chem. Lett.* **2015**, *6*, 4073.
30. Yang, N.; Waldvogel, S. R.; Jiang, X.; *ACS Appl. Mater. Interfaces* **2016**, *8*, 28357.
31. Jermann, B.; Augustynski, J.; *Electrochim. Acta* **1994**, *39*, 1891.
32. Peterson, A. A.; Nørskov, J. K.; *J. Phys. Chem. Lett.* **2012**, *3*, 251.
33. Hansen, H. A.; Shi, C.; Lausche, A. C.; Peterson, A. A.; Nørskov, J. K.; *Phys. Chem. Chem. Phys.* **2016**, *18*, 9194.
34. Liu, X.; Wang, D.; Li, Y.; *Nano Today* **2012**, *7*, 448.
35. Mistry, H.; Reske, R.; Strasser, P.; Roldan Cuenya, B.; *Catal. Today* **2016**, *22*, 54.
36. Guo, X.; Zhang, Y.; Deng, C.; Li, X.; Xue, Y.; Yan, Y.; Sun, K.; *Chem. Commun.* **2015**, *51*, 1345.
37. Grote, J.; Zeradjanin, A. R.; Cherevko, S.; Savan, A.; Breitbach, B.; Ludwig, A.; Mayrhofer, K. J. J.; *J. Catal.* **2016**, *343*, 248.
38. Monzó, J.; Malewski, Y.; Kortlever, R.; Vidal-Iglesias, F. J.; Solla-Gullón, J.; Koper, M. T. M.; Rodriguez, P.; *J. Mater. Chem. A* **2015**, *3*, 23690.
39. Sarkar, A.; Manthiram, A.; *J. Phys. Chem. C* **2010**, *114*, 4725.
40. Zhang, J.; Lima, F. H. B.; Shao, M. H.; Sasaki, K.; Wang, J. X.; Hanson, J.; Adzic, R. R.; *J. Phys. Chem. B* **2005**, *109*, 22701.
41. Kiros, Y.; *J. Electrochem. Soc.* **1996**, *143*, 2152.
42. Corradini, P. G.; Santos, N. A.; Silva, G. C.; Perez, J.; *J. Solid State Electrochem.* **2016**, *20*, 2581.

43. McBreen, J.; O'Grady, W. E.; Pandya, K. I.; Hoffman, R. W.; Sayers, D. E.; *Langmuir* **1987**, *3*, 428.
44. Ravel, B.; Newville, M.; *J. Synchrotron Radiat.* **2005**, *12*, 537.
45. Baltruschat, H.; *J. Am. Soc. Mass Spectrom.* **2004**, *15*, 1693.
46. Wolter, O.; Heitbaum, J.; *Ber. Bunsenges. Phys. Chem.* **1984**, *88*, 2.
47. Clark, E. L.; Singh, M. R.; Kwon, Y.; Bell, A. T.; *Anal. Chem.* **2015**, *87*, 8013.
48. Roberts, F. S.; Kuhl, K. P.; Nilsson, A.; *Angew. Chem., Int. Ed.* **2015**, *54*, 5179.
49. Javier, A.; Chmielowiec, B.; Sanabria-Chinchilla, J.; Kim, Y.; Baricuatro, J. H.; Soriaga, M. P.; *Electrocatalysis* **2015**, *6*, 127.
50. Venkatachalam, S.; Angelici, R. J.; Woo, L. K.; Hillier, A. C.; *Anal. Chem.* **2013**, *85*, 6059.
51. Sousa, R.; Colmati, F.; Ciapina, E. G.; Gonzalez, E. R.; *J. Solid State Electrochem.* **2007**, *11*, 1549.
52. Gonçalves, M. R.; Gomes, A.; Condeço, J.; Fernandes, R.; Pardal, T.; Sequeira, C. A. C.; Branco, J. B.; *Energy Convers. Manage.* **2010**, *51*, 30.
53. Chen, C. S.; Handoko, A. D.; Wan, J. H.; Ma, L.; Ren, D.; Yeo, B. S.; *Catal. Sci. Technol.* **2015**, *5*, 161.
54. Bard, A.; Faulkner, L.; *Electrochemical Methods: Fundamentals and Applications*; John Wiley & Sons, Inc.: New York, USA, 2001.
55. Zhang, N.; Chen, X.; Lu, Y.; An, L.; Li, X.; Xia, D.; Zhang, Z.; Li, J.; *Small* **2014**, *10*, 2662.
56. Zhang, S.; Shao, Y.; Liao, H. G.; Liu, J.; Aksay, I. A.; Yin, G.; Lin, Y.; *Chem. Mater.* **2011**, *23*, 1079.
57. Yin, J.; Shan, S.; Ng, M. S.; Yang, L.; Mott, D.; Fang, W.; Kang, N.; Luo, J.; Zhong, C. J.; *Langmuir* **2013**, *29*, 9249.
58. Zhao, Y.; Wang, C.; Wallace, G. G.; *J. Mater. Chem. A* **2016**, *4*, 10710.
59. Lima, F. H. B.; Profeti, D.; Chatenet, M.; Riello, D.; Ticianelli, E. A.; Gonzalez, E. R.; *Electrocatalysis* **2010**, *1*, 72.
60. Sarfraz, S.; Garcia-Esparza, A. T.; Jedidi, A.; Cavallo, L.; Takanabe, K.; *ACS Catal.* **2016**, *6*, 2842.
61. Fujihira, M.; Noguchi, T.; *Chem. Lett.* **1992**, *21*, 2043.
62. Shen, J.; Kortlever, R.; Kas, R.; Birdja, Y. Y.; Diaz-Morales, O.; Kwon, Y.; Ledezma-Yanez, I.; Schouten, K. J. P.; Mul, G.; Koper, M. T. M.; *Nat. Commun.* **2015**, *6*, 8177.
63. Wasmus, S.; Cattaneo, E.; Vielstich, W.; *Electrochim. Acta* **1990**, *35*, 771.
64. Hori, Y. In *Modern Aspects of Electrochemistry*; Vayenas, C. G.; White, R. E.; Gamboa-Aldeco, M. E., eds.; Springer New York: New York, NY, USA, 2008, p. 89.
65. Qiao, J.; Liu, Y.; Hong, F.; Zhang, J.; *Chem. Soc. Rev.* **2014**, *43*, 631.
66. Ren, D.; Deng, Y.; Handoko, A. D.; Chen, C. S.; Malkhandi, S.; Yeo, B. S.; *ACS Catal.* **2015**, *5*, 2814.
67. DeWulf, D. W.; Jin, T.; Bard, A. J.; *J. Electrochem. Soc.* **1989**, *136*, 1686.
68. Smith, B. D.; Irish, D. E.; Kedzierzawski, P.; Augustynski, J.; *J. Electrochem. Soc.* **1997**, *144*, 4288.
69. Baruch, M. F.; Pander, J. E.; White, J. L.; Bocarsly, A. B.; *ACS Catal.* **2015**, *5*, 3148.
70. Watanabe, M.; *J. Electrochem. Soc.* **1991**, *305*, 319.
71. Kedzierzawski, P.; Augustynski, J.; *J. Electrochem. Soc.* **1994**, *141*, L58.
72. Shi, J.; Li, Q. Y.; Shi, F.; Song, N.; Jia, Y. J.; Hu, Y. Q.; Shen, F.; Yang, D.; Dai, Y. N.; *J. Electrochem. Soc.* **2016**, *163*, G82.

Submitted: January 18, 2016
Published online: March 31, 2017